2018 7th IEEE International Conference on Biomedical
Robotics and Biomechatronics (Biorob)
Enschede, The Netherlands, August 26-29, 2018

Numerical simulations and development of drafting strategies for robotic swimmers at low Reynolds number

Caroline Bernier[1], Mattia Gazzola[2], Philippe Chatelain[1] and Renaud Ronsse[1]

Abstract— **The emergence and understanding of new design principles that exploit flow-induced mechanical instabilities for propulsion require robust and accurate flow-structure interaction numerical models. In this contribution, we report the development of an algorithm that combines Vortex Particles Mesh (VPM) method and Multi-Body System (MBS) solver for the simulation of actuated swimming structures in fluids. The hydrodynamic efforts are recovered through an innovative approach based on the penalization and projection steps performed within the VPM method. The resulting method avoids time consuming computation of the stresses at the wall to recover the force distribution on the surface of complex deforming shapes. This feature crucially distinguish the proposed approach from other VPM formulations and opens the door for the development of control frameworks for bio-inspired and autonomous robotic swimmers. As a first illustration towards this goal, this paper reports a swimming agent stabilizing its gait in the wake of a cylinder. Illustrating the dynamic features of our framework, we report the energy saved by swimming behind this cylinder as compared to a stationary gait in an induced flow. We also compared this result to the energy saved by following the wake of a moving cylinder.**

I. Introduction

The thorough comprehension of biological locomotion in fluids promises great advances in hydrodynamics, flow control, and efficient underwater vehicles (UVs) propulsion. Nowadays UVs are thrust by means of propellers: those are barred from achieving high efficiency due to the high velocities, hence energy losses, in the jets being produced.

A closer look at fish swimming techniques, for instance anguilliform ones, reveals that undulatory gaits achieve higher efficiency because of effective linear momentum transfer to the flow in the forward direction [1]. Moreover, fish can sense the flow in order to adapt their gait to unsteady conditions and exploit beneficial flow structure. Such behaviors have only recently begun to be uncovered by biologists and engineers alike [2]. An intuitive illustration is represented by the energy saving behavior of fishes resting behind rocks in rivers [3]. On the way to reproduce and understand such intriguing flow-structure interplay, an increasing number of robotic platforms emerged in the last decades [4], [5], [6].

Numerical flow solvers have also been applied to self-propelled swimmers in order to investigate swimming gaits and bio-inspired sensorimotor mechanisms. Several methods were proposed, ranging from quasi-analytical theoretical models in potential flow [7], [8], [9] to more computationally-intensive numerical methods for viscous flows [10], [11]. Interestingly, very few can actually be used to study self-propelled structures, their actuation principles, and their dynamical control in a unified framework [12], [6], [13]. We recently paved the way towards such a framework, by developing a penalized Vortex Particle-Mesh (VPM) method coupled to a Multi-Body System (MBS) solver. This framework enables to simulate actuated swimmers interacting with unsteady, complex environments [13].

In the present paper, we extend this methodology to the development of a controller that allows a swimmer to draft behind an obstacle. Such a behavior is actually a simplified version of collective motions in actual school of fish, where the individuals are believed to exploit flow structures generated by their neighbors [14], [15]. In our simulations, the virtual swimmer entails articulated rigid bodies and flow sensors, which are used to track the wake of a cylinder in a uniform flow. We investigate the energy saving through this drafting technique by comparing its cost to that of stationary gait in an uniform flow. We also assess the performance of the drafting technique if the wake generator is moving in order to reproduce a leader-follower scenario.

The rest of this paper is structured as follows. Section II overviews our framework combining the VPM fluid solver and the MBS. In Section III, the setup, controllers and parameters used in simulations are presented. Section IV reports the results of our simulations. A discussion of the results is developed in Section V. Finally, concluding remarks are reported in Section VI.

II. Coupled solver overview

The simulation of a two-dimensional articulated structure in a complex flow environment is performed by means of a new approach presented in [13]. This method relies on a Vortex Particle-Mesh (VPM) method with penalization and a Multi-Body System (MBS) solver. In this section, we review its main features.

A. Vortex method for fluid structure interaction

The VPM method solves incompressible flows using the vorticity-velocity formulation of the Navier-Stokes equations, i.e.:

$$\frac{D\omega}{Dt} = (\omega \cdot \nabla)\,\mathbf{u} + \nu \nabla^2 \omega \tag{1}$$

where $\frac{D}{Dt} = \frac{\partial}{\partial t} + \mathbf{u} \cdot \nabla$ denotes the Lagrangian derivative, $\mathbf{u}$ is the velocity field, ω the vorticity field and ν the kinematic

[1]Institute of Mechanics, Materials and Civil Engineering (iMMC), Université catholique de Louvain (UCL), 1348 Louvain-la-Neuve, Belgium caroline.bernier@uclouvain.be

[2]Mechanical Science and Engineering, University of Illinois at Urbana-Champaign, USA

978-1-5386-8183-1/18/$31.00 ©2018 IEEE

viscosity. The velocity field is recovered from the vorticity by solving the Poisson equation:

$$\nabla^2 \mathbf{u} = -\nabla \times \omega \,. \tag{2}$$

The advection of vorticity is handled in a Lagrangian fashion using particles, characterized by a position $\mathbf{x}_p$, a volume V_p and a vorticity integral $\alpha_p = \int_{V_p} \omega d\mathbf{x}$, i.e.:

$$\frac{d\mathbf{x}_p}{dt} = \mathbf{u}_p \tag{3}$$

$$\frac{d\alpha_p}{dt} = \left((\omega \cdot \nabla)\mathbf{u} + \nu \nabla^2 \omega\right)_p \,, \tag{4}$$

where we identify the roles of the velocity field in the advection in Eq. (3), and of the vortex stretching and diffusion for the evolution of vorticity in Eq. (4). This stretching term will be omitted in the rest of this article, because it is only non-zero in three dimensions while our implementation and test cases are all two dimensional. The method adapts the time step according to a Lagrangian CFL condition (LCFL) for the explicit time integration of advection [16]. In order to capture the complex interaction between the fluid and the solid, we combine two techniques: the Brinkman penalization and the projection technique.

1) Brinkman penalization: The shapes and positions of the immersed bodies are described by a mollified characteristic function, χ_s constructed upon the level set description of the geometries (see [11] for further details).

The boundary condition enforcement itself is performed by means of the Brinkman penalization technique. This approach extends the fluid domain into the solid region and thus considers the fluid and solid as a global continuous domain Υ, combining the solid surface Ω and the fluid surface Σ. The enforcement of the no-slip boundary condition is achieved by the addition of a term that drives the fluid velocity $\mathbf{u}$ inside the solid region to a prescribed body velocity $\mathbf{u}_s$. The penalized Navier-Stokes equations then read

$$\frac{D\mathbf{u}}{Dt} = -\frac{1}{\rho}\nabla p + \nu \nabla^2 \mathbf{u} + \lambda \chi_s (\mathbf{u}_s - \mathbf{u}), \ \mathbf{x} \in \Upsilon \tag{5}$$

where $\lambda \gg 1$ is the penalization factor and $\lambda \chi_s(\mathbf{u}_s - \mathbf{u})$, the penalization term. λ can be fixed at an arbitrary value, which directly governs the error in the penalized solution, i.e.: $||\mathbf{u} - \mathbf{u}_\lambda|| \leq C\lambda^{-1/2}||\mathbf{u}||$. High values enforce the wall boundary condition more strictly, although at the cost of a stiffer term that needs to be integrated in time. Note that in our VPM method, the curl of this equation is actually advanced in time.

2) Projection technique: The projection technique captures the action of the fluid on the solid body. First, at each time step, the fluid evolves freely over the whole domain – i.e. as if no body was there – according to the current velocity field. The outcome of this first step is an intermediate state, denoted as *star* state. The resulting extended flow field $\mathbf{u}_*$ violates the rigid motion of the immersed body. Over this intermediate step, the domain region described by the characteristic function of a body acquires a new momentum integral which correctly captures the flux of momentum between the fluid and the body (for detailed proof, see [17]). This newly acquired momentum is finally translated into rotational and translational velocities of the body which are enfoced upon the flow by the penalization method so as to regain physical consistency after the *star* state. We refer to [11] for a thorough description of this method.

B. Extension to an articulated system

In order to treat an articulated system of solid elements with embedded actuation, a MBS solver is added to the fluid solver to predict the deformation of the immersed articulated structure. In this section, we detail and discuss the components of this extension: the description of the articulated structure, the multi-body system (MBS) solver and the computation of the hydrodynamic efforts from the penalization (Section II-A.1) and projection (Section II-A.2) schemes.

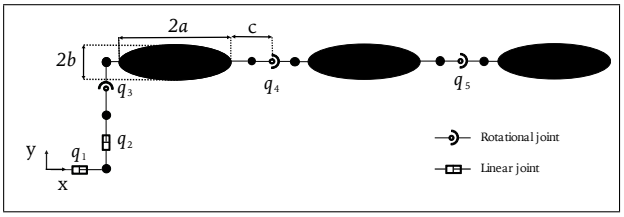

Fig. 1. Multi-body diagram of a 3 bodied eel-like structure: floating base generalized coordinates, q_1, q_2, q_3, and joints generalized coordinates, q_4, q_5. For each segment, $2a$ is equal to the length, $2b$ to the width and c to the distance from the tip to the next joint.

1) Free articulated system: We consider a two-dimensional MBS composed of N linked rigid bodies, here elliptical elements, immersed in a fluid (Fig. 1 for an example with $N = 3$) and connected by means of virtual joints, all rotational in our case. Each joint entails a degree of freedom that is represented by a generalized coordinate q_i, i.e. the angle between two successive elements. The first three coordinates, q_1, q_2, q_3, (2 linear and 1 rotational coordinates) describe the motion of the floating base, providing the three degrees of freedom related to translations and rotation in the $\mathbf{x}$, $\mathbf{y}$ plane. The articulated structure configuration is then described by a set of generalized coordinates: $\mathbf{q} = [q_1 \ q_2 ... \ q_n]^T$, with $n = N + 2$ in the present case. The footprint of the structure in space is then described by a set of characteristic functions, $\chi_{s,j}$, each one representing an elliptical element j.

2) Multi-body dynamics equations: In this section, we establish the dynamical equations governing the actuated structure. The linear and angular velocities of each body j, $\mathbf{v}_{c,j}$ and $\omega_{c,j}$, are measured with respect to its center of mass and are computed from the generalized coordinates as

$$\mathbf{v}_{c,j} = \mathbf{J}_{v,j}(\mathbf{q})\,\dot{\mathbf{q}} \tag{6}$$

$$\omega_{c,i} = \mathbf{J}_{\omega,j}(\mathbf{q})\,\dot{\mathbf{q}} \tag{7}$$

where $\mathbf{J}_{v,j}(\mathbf{q})$ and $\mathbf{J}_{\omega,i}(\mathbf{q})$ are the Jacobian matrices associated to the linear and angular velocities, respectively. Following a classical approach from robotics [18], we derive the governing equations for the whole system dynamics

through the Euler-Lagrange formalism. The complete dynamical system is then described by the following set of equations:

$$\mathbf{D}(\mathbf{q})\ddot{\mathbf{q}} + \mathbf{C}(\mathbf{q},\dot{\mathbf{q}})\dot{\mathbf{q}} = \tau \tag{8}$$

where $\mathbf{D}(\mathbf{q})$ is the inertia matrix, i.e.:

$$\mathbf{D}(\mathbf{q}) = \sum_{j=1}^{N} \left\{ m_i \mathbf{J}_{v,j}^T \mathbf{J}_{v,j} + \mathbf{J}_{\omega,j}^T \mathbf{R}_j(\mathbf{q}) \mathbf{I}_j \mathbf{R}_j^T(\mathbf{q}) \mathbf{J}_{\omega,i} \right\} \tag{9}$$

where we dropped the explicit dependencies of the matrices $\mathbf{J}_{v,j}$ and $\mathbf{J}_{\omega,j}$ on $\mathbf{q}$ for the sake of clarity, m_j is the mass of body j, $\mathbf{I}_j$ its inertia about a frame fixed to its center of mass, and $R_j(\mathbf{q})$, the rotation matrix capturing the body orientation with respect to the inertial frame. The matrix $\mathbf{C}(\mathbf{q},\dot{\mathbf{q}})$ gathers the Coriolis and centrifugal forces; its elements being given by

$$C_{lm} = \sum_{i=1}^{n} \frac{1}{2} \left\{ \frac{\partial D_{lm}}{\partial q_i} + \frac{\partial D_{li}}{\partial q_m} - \frac{\partial D_{im}}{\partial q_l} \right\} \dot{q}_i \,. \tag{10}$$

Finally, τ is the vector of efforts applied to each joint and is defined as

$$\tau = \tau_{\text{hyd}} + \tau_{\text{act}} \tag{11}$$

where τ_{hyd} is the effort due to the hydrodynamic forces and torques applied to the segments and τ_{act} is the actuation effort transmitted to the body. For a rotational joint i, τ_i captures the applied torque and for a linear one, it is the force collinear to the joint direction.

3) Fluid-structure interaction efforts: We recover the hydrodynamic forces and moments on each segment j from the penalization and projection steps of the fluid solver. One can indeed consider momentum conservation for the material volumes spanned by the bodies, i.e.:

$$\mathbf{F}_{\text{hyd},j} = \frac{D}{Dt} \int_{\Omega_j} \rho \mathbf{u} \; dV + \int_{\Omega_j} \rho \lambda \chi_s (\mathbf{u} - \mathbf{u}_s) \; dV, \tag{12}$$

$$\mathbf{M}_{\text{hyd},j} = \frac{D}{Dt} \int_{\Omega_j} \rho \; (\mathbf{x} \times \mathbf{u}) \; dV + \int_{\Omega_j} \mathbf{x} \times (\rho \lambda \chi_s (\mathbf{u} - \mathbf{u}_s)) \; dV \,. \tag{13}$$

The resulting efforts, $\mathbf{F}_{hyd}$ and $\mathbf{M}_{\text{hyd}}$, are each composed of two terms. The present approach will perform the evaluation of the time derivatives of the first term, while the second term is straightforwardly identified as the contribution due to the penalization technique. Note that the moment $\mathbf{M}_{\text{hyd}}$ is computed with respect to the origin; it still needs to be translated to the body center of mass $\mathbf{x}_{\text{cm}}$ through $\mathbf{M}_{\text{hyd, cm}} = \mathbf{M}_{\text{hyd}} - \mathbf{x}_{\text{cm}} \times \mathbf{F}_{\text{hyd}}$ in order to be used in the MBS solver (see Section II-B.2).

III. Drafting benchmark: gait generation, control and sensing

In this section, we describe a bio-inspired control framework aimed at tracking a wake structure to achieve energy savings. We consider the evolution of a swimmer's configuration in the wake generated by a uniform flow past a cylinder (fixed or moving). Indeed the flow past a cylinder features a wake region, characterized by velocities favorable to the swimmer, increasing its propulsion efficiency. However, the swimmer has to stay close to the cylinder in order to exploit this wake.

We focus on a case where a cylinder of diameter D and a four-element swimmer interact in a uniform free stream of velocity U (Fig. 2). The passive swimmer is neutrally buoyant and located at a distance d downstream of the cylinder at the beginning of each simulation. The swimmer is composed of four segments, each characterized by $2a = 0.625D$, $b = 0.1a$ and $c = 0.1D$ (Fig. 1).

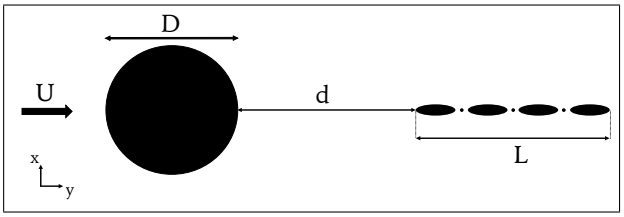

Fig. 2. Simulation setup: cylinder of diameter D and a four-elements swimmer of total length L. The incoming uniform stream flow has a velocity equal to U.

In order to feel the flow, the swimmer is equipped with virtual antennas attached to its head at a distance $d_a = 2a$ of its front segment (Fig. 3). The antennas provide an absolute measurement of the flow vorticity (i.e. $\omega = \nabla \times \mathbf{u}$) V_R and V_L.

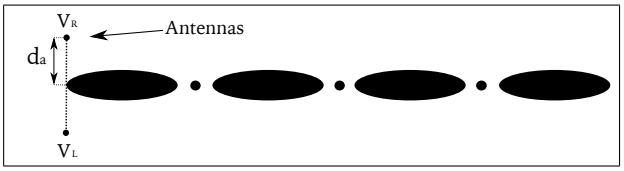

Fig. 3. The swimmer is equipped with virtual antennas measuring the vorticity on the right V_R and on the left V_L of its first segment.

In the remainder of this section, we develop three nested control laws that are combined in order to stabilize the swimmer in the wake.

A. Propulsion controller

The fish is propelled by imposing an eel-like movement to its body, so that the elements generalized coordinates follow the trajectory given by:

$$\begin{aligned} &\text{For } i = 4, ..., N+2 \; : \\ &q_{i,ref} \;=\; \alpha \; \frac{s_i}{L + 0.25} \quad \sin\left(2\pi \left(\omega_f t + \tfrac{s_i}{L+0.25}\right)\right), \end{aligned} \tag{14}$$

where α is the motion amplitude, L is the length of the fish, s_i is the position of the joint i along the body and ω_f is the global movement angular frequency.

Kinematic tracking is achieved through a simple proportional controller, i.e.:

$$\tau_i = K_{prop}(q_{i,ref} - q_i). \tag{15}$$

Expressed in dimensionless form, this proportional gain is taken equal to $K'_{prop} = \frac{K_{prop}}{\rho U^2 D} = 10$ in all reported simulations.

B. Position controller

The distance to the cylinder, d is controlled via the the overall movement amplitude, α, in Eq. (14). This parameter makes the swimmer moving faster or slower. The close-loop controller is achieved through the use of a saturated PI controller combined with an anti-windup loop. The coefficients of this controller are the gains K_p and K_i, and the saturation limit S. These gains are adjusted according to the application scenarios that were tested (see Section IV).

C. Steering controller

Finally, the steering controller is in charge of maintaining the swimmer aligned with the cylinder motion relative to the fluid and within the shed vortices, through virtual sensory inputs collected by both antennas. The instantaneously measured values are first filtered through a second-order exponential smoothing filter with a cutoff frequency f_f. The filtered signal are denoted as $\overline{V}_R$ and $\overline{V}_L$. Steering is achieved by modulating the reference motion of the generalized coordinates by

$$q_{i,ref2} = q_{i,ref} + C_v, \tag{16}$$

with C_v being the desired body curvature. This curvature is controlled towards achieving balancing of the absolute vorticities sensed by the the left and right antennas, thus driving the swimmer to an alignment with the vortex shedding:

$$C_v = K_s(\overline{V}_R - \overline{V}_L). \tag{17}$$

Altogether, the three control loops thus drive the swimmer to maintain a position within the wake of the cylinder and thus should contribute to decrease the energy spent for its locomotion.

D. Simulations parameters

Simulations are computed on a domain with a size of $[0;13.2D]\times[0;6.6D]$ and discretized by a 512×256 grid. The cylinder diameter is taken equal to 0.2 m, its rest position being located at $(1.98D,\ 3.3D)$. The following numerical parameters for VPM and the penalization are used: $LCFL = 2.10^{-2}$, $\varepsilon = 2h_{512}$, $\lambda = 1.10^{-4}$ where h_{512} is the spacing of the uniform grid.

The Reynolds number is set equal to $Re = \frac{UD}{\nu} = 100$ and the Strouhal number for the cylinder alone is found to be $St = \frac{f_c D}{U} = 0.23$, with f_c the shedding frequency. We chose the angular frequency of the imposed coordinates trajectory to be high compared to the frequency of shedding, i.e. $\omega_f = 2\pi f = 24\pi f_c$. This higher frequency allows the swimmer to maneuver within the wake vortices and track their motion adequately.

All simulations start with an initial phase ($t' = \frac{tU}{D} \leqslant t'_{start}$) during which the swimmer is held stationary. This initial phase also contains a perturbation to accelerate the transition to the periodic shedding of vortices by the cylinder. This perturbation, which happens for $t' \leqslant 4$, consists in a rotation of the cylinder at an angular velocity $\Omega = \sin(0.125\pi t')$. The remainder of the initial phase allows the shedding to reach its periodic regime and the shed vortices to interact with the still fixed swimmer.

IV. Results

In this section, the controllers derived above are validated on three distinct test cases: a swimmer maintaining a stationary position in a uniform flow without a cylinder (1), evolving behind a stationary cylinder (2), and evolving behind a moving cylinder (3). The resulting dynamics are presented in the video attached to this paper.

Table I gathers the values of the controller coefficients for all the test cases; they are provided in dimensionless form for the sake of generality.

TABLE I
DIMENSIONLESS CONTROLLER COEFFICIENTS (FOR CASE (1) $K''_s = K'_s D$)

Cases	$K'_i = \frac{K_i D^2}{U}$	$K'_p = K_p D$	$K'_s = \frac{K_s D}{U}$	S	$f'_f = \frac{f_f D}{U}$
(1)	0.6	6	1.4	2.5	/
(2)	0.6	3	0.2	1.5	0.15
(3)	0.6	4	1	2.5	0.063

A. Position holding in a uniform flow

In this test case, we did not use the steering controller from Eq. (17), since there was no vorticity upstream of the swimmer. Instead, a proportional controller canceling the difference of vertical position between the swimmer and the reference was used to compute C_v:

$$C_v = K''_s(y(t) - y_{ref})$$

The swimmer goal was thus to remain centered at y_{ref}.

Figure IV-A reveals that the swimmer reached its reference position at the center of the domain in about 40 dimensionless time units. The average dimensionless power produced by the three joints was equal to $\overline{P}' = \frac{\overline{P}}{\rho U^3 D} = 15.05$ where $P = \sum_{i=4}^{6} \tau_i \dot{q}_i$ is the actuation power. This average was calculated when the swimmer reached its steady position and movement, i.e. when $t' \geqslant 50$.

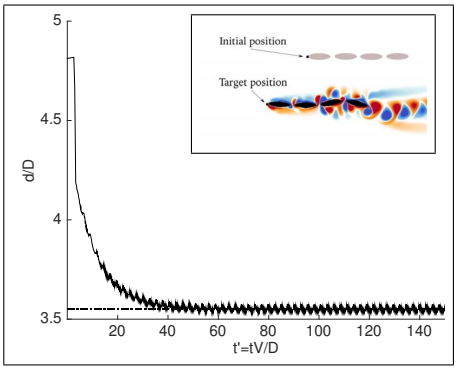

Fig. 4. Position holding in uniform flow: horizontal position of the first segment center of mass (solid) and reference value (dashed). Vorticity snapshot at $t' = tU/D = 40$.

B. Stationary cylinder wake tracking

Figure 6(a) shows the results of the three nested controllers presented in Section III thus combining the stabilization of

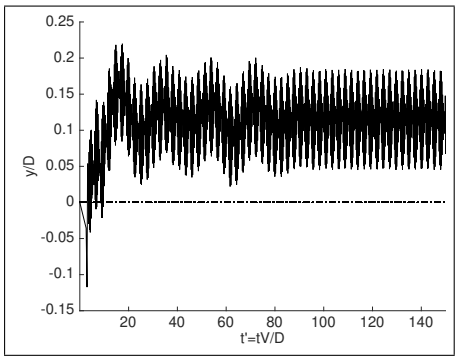

Fig. 5. Position holding in uniform flow: vertical position of the first segment center of mass (solid) and reference value (dashed).

distance to the cylinder, and flow exploitation. It reveals that the swimmer reached its stationary position, $d_{ref} = 3.5D$, in the horizontal direction in about 10 dimensionless time and with no overshoot. Regarding the y direction, Fig. 6(b) reveals that the swimmer oscillated around the reference position, i.e. the one of the cylinder. The amplitude of these oscillations is about 0.7D. The average dimensionless power produced by the three articulated joints is equal to $\overline{P}' = 12.94$. This average was computed when the swimmer reached its steady position with respect to the cylinder, i.e. when $t' \geqslant 22$. The average power is thus 14% smaller as compared to the first case where the swimmer did not interact with vortical perturbations to maintain its stationary position.

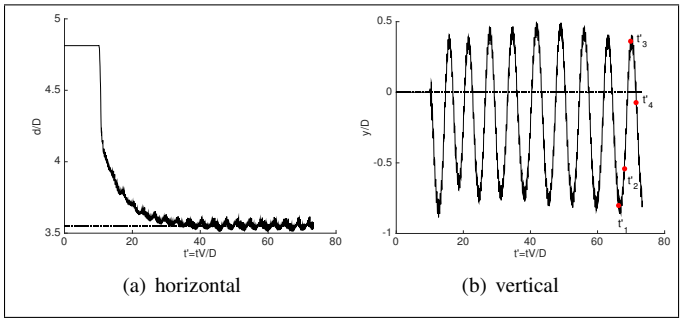

(a) horizontal (b) vertical

Fig. 6. Stationary cylinder wake tracking: position of the first segment center of mass (solid) and reference value (dashed).

Figure 7 shows the vorticity contour around the swimmer when it stabilized in the wake.

C. Moving cylinder wake tracking

Here the kinematic of the cylinder is imposed to follow a vertical motion captured by:

$$y_{cyl}(t) = \alpha_{cyl} \sin(2\pi f_{cyl} t)$$

where $\alpha_c yl' = \frac{\alpha_{cyl}}{D} = 1.5$ is the dimensionless amplitude and $f'_{cyl} = \frac{f_{cyl} D}{U} = 0.066$ the dimensionless frequency of this motion.

Again the swimmer reaches its reference distance to the cylinder $d_{ref} = 3.5D$, although with larger oscillations as in the previous case, since the cylinder itself is oscillating. The average power in this case is $\overline{P}' = 14.01$. This was calculated

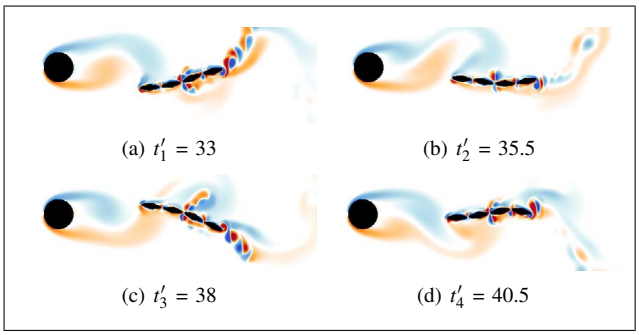

Fig. 7. Stationary cylinder wake tracking: vorticity snapshots at different normalized times: $t' = tU/D$ taken in the last period of the regime movement of the swimmer (Fig.6(b)). Negative and positive vorticity are denoted in blue and red respectively.

when the swimmer reached its steady position with respect to the cylinder, i.e. when $t' \geqslant 30$. Again the power consumed to stabilize behind the moving cylinder is 7% smaller as compared to swimming in a uniform flow.

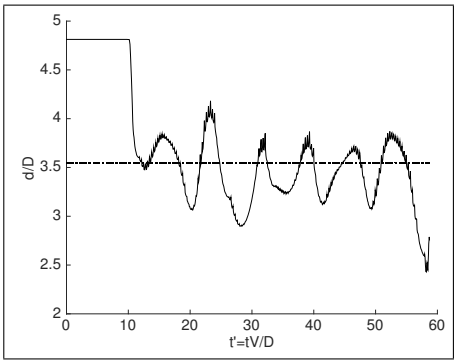

Fig. 8. Moving cylinder wake tracking: horizontal position of the first segment center of mass (solid) and reference value (dashed).

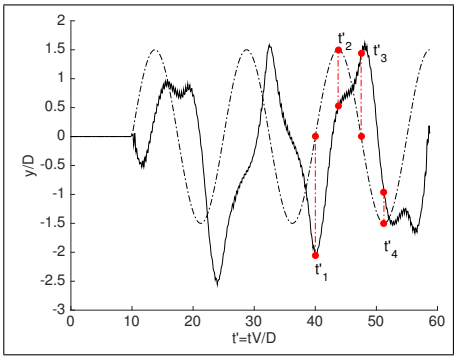

Fig. 9. Moving cylinder wake tracking: vertical position of the first segment center of mass (solid) and of the cylinder (dashed).

Fig. 10 shows the vorticity plot around the swimmer when stabilized in the wake.

V. Discussion

Wakes involve very specific vortical structures (vortices, sheets, tubes) which can subject a downstream device to substantial forces [3], [19]. In the specific case of a cylinder

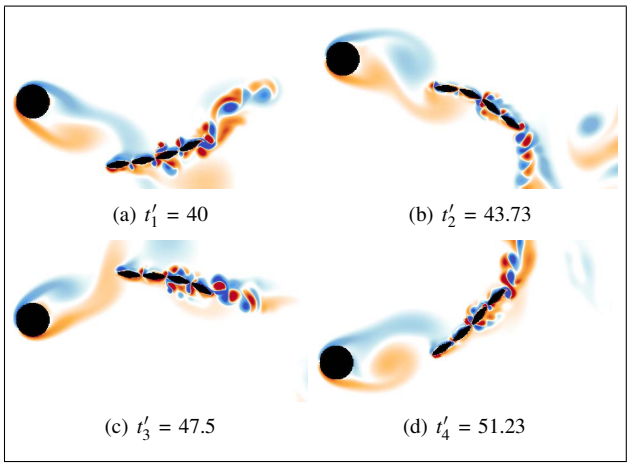

Fig. 10. Moving cylinder wake tracking: vorticity snapshots at different normalized times: $t' = tU/D$ taken in the last period of the regime movement of the swimmer (Fig.9). Colors are similar as in Fig. 7.

subject to an incoming flow at low Reynolds number, a von Kàrmàn vortex street is generated. This wake structure involves a low pressure region directly behind the cylinder and the shedding of well-separated vortices with alternating strengths. We have shown in the previous section that it is possible, through a specific motion within the vortex street, to reduce the mean power required to propel the swimming device. The efficient exploitation of the shed vortical structures requires that the swimmer remains both synchronized with the vortex shedding and close to the cylinder. The last test case illustrates these requirements in a counter-example: the swimmer does not manage to stabilize well enough in the wake and loses most of the drafting benefit. The resulting tracking performance of the control algorithm is thus of paramount importance to stay synchronized with the vortical structures.

VI. Conclusions

In this paper, we have developed a bio-inspired control framework for self-propelled swimmers evolving in complex flows. This framework relies on three nested control layers and was validated through a unique fluid-structure interaction algorithm achieving simultaneous dynamical simulations of the fluid, the body, and its controller.

The resulting approach has been applied to several scenarios of increasing complexity. The swimmer indeed had to maintain a stationary position in a uniform flow or exploit the wake of an obstacle, which was first stationary then mobile. Results showed that the swimmer saved $7-15\%$ energy when it evolved within a wake rather than in a uniform flow.

This work paves the way towards more complex energy efficient bio-inspired frameworks in complex flow scenarios, which could include many devices interacting through their wakes. Bio-inspired sensing mechanism measuring velocity or pressure along the body length could also be added to the swimmer in order to enhance its perception of the environment. This enhanced sensory apparatus could then be used to follow a specific stream or perturbations created by obstacles. The topic of bio-sensory mechanisms and the subsequent use of the perceived information is still an open problem in biology and engineering: the present simulation environment, which covers flow dynamics, device dynamics and their control, enables, for the first time, the assessment of sensory and control hypotheses for biological or bio-inspired systems.

Acknowledgments

The present research benefited from computational resources made available on the Tier-1 supercomputer of the Fédération Wallonie-Bruxelles, infrastructure funded by the Walloon Region under the grant agreement n^{o}1117545. Caroline Bernier was funded by a FSR fellowship of Université catholique de Louvain for the project COMPACTSWIM (FSR 2013).

References

[1] M. Gazzola, M. Argentina, and L. Mahadevan, Scaling macroscopic aquatic locomotion, in Nature Physics, vol. 10, pp. 758-761, 2014.
[2] J. O. Dabiri, How fish feel the flow, in Nature, vol. 547, pp. 406-407, 2017.
[3] D. N. Beal, F. S. Hover, M. S. Triantafyllou, J. C. Liao and George V. Lauder, Passive propulsion in vortex wakes, in JFM, vol. 549, pp. 385-402, 2006.
[4] A. J. Ijspeert, Biorobotics: Using robots to emulate and investigate agile locomotion, in Science, vol. 346, pp. 196-203, October 2014.
[5] E. Kelasidi, P. Liljebäck, K. Pettersen and T. Gravdhal, Biologically inspired snake robot, in IEEE Robotics & Autom. Mag., vol. 23, pp. 44-62, 2016.
[6] M. Porez, F. Boyer, A. J. Ijspeert, Improved lighthill fish swimming model for bio-inspired robots-modelling, computational aspects and experimental comparisons, in International Journal of Robotics Research, SAGE Publications, pp.1-34, 2014.
[7] M. J. Lighthill, Note on the swimming of slender fish, in JFM, vol. 9, pp. 305-317, 1960.
[8] J. Lighthill, Large-amplitude elongated body theory of fish locomotion, in Proceedings of the Royal Society B, vol. 179, pp. 125-138, 1971.
[9] E. Kanso, J. E. Marsden, C. W. Rowley and J. Melli-Huber, Locomotion of articulated bodies in a perfect fluid, in JNS, vol. 15, pp. 255-289, 2005.
[10] A. Gilmanov and F. Sotiropoulos, A hybrid Cartesian/immersed boundary method for simulating flows with 3D, geometrically complex, moving bodies, in JCP, vol. 207, pp. 457-492, 2005.
[11] M. Gazzola, P. Chatelain, W. M. van Rees and P. Koumoutsakos, Simulations of single and multiple swimmers with non-divergence free deforming geometries, in JCP, vol. 230, pp. 7093-7114, 2011.
[12] F. Boyer, M. Porez, A. Leroyer, Poincaré-cosserat equations for lighthill three-dimensional dynamic model of a self propelled eel devoted to robotics, in JNS, vol. 20, pp. 47-79, 2010.
[13] C. Bernier, M. Gazzola, R. Ronsse and P. Chatelain, Simulations of propelling and energy harvesting articulated bodies via vortex particle-mesh methods, in ArXiv e-prints, eprint 1805.10691, 2018.
[14] D. Weihs, Hydromechanics of fish schooling, in Nature, vol. 241, pp. 290-291, 1973.
[15] M. Gazzola, A. Tchieu, D. Alexeev, A. De Brauer and P. Koumoutsakos, Learning to school in the presence of hydrodynamic interactions, in JFM, vol. 789, pp. 726-749, 2016.
[16] P. Koumoutsakos, Multiscale flow simulations using particles, in Annual Review of Fluid Mechanics, vol. 37, pp. 457-487, 2005.
[17] N. A. Patankar and N. Sharma, A fast projection scheme for the direct numerical simulation of rigid particulate flows, in Communications in Numerical Methods in Engineering, vol. 21, pp. 419-432, 2005.
[18] M.W. Spong, S. Hutchinson and M.Vidyasagar, Robot Modeling and Control, John Wiley & Sons, Inc., 2006.
[19] J. D. Eldredge and David Pisani, Passive locomotion of a simple articulated fish-like system in the wake of an obstacle, in Journal of Fluid Mechanics, vol. 607, pp. 279-288, 2008.